

Fabrication of Elliptical Nanorings with Highly Tunable and Multiple Plasmonic Resonances

Yangjun Cai,[†] Yang Li,[‡] Peter Nordlander,[‡] and Paul S. Cremer^{*,†}

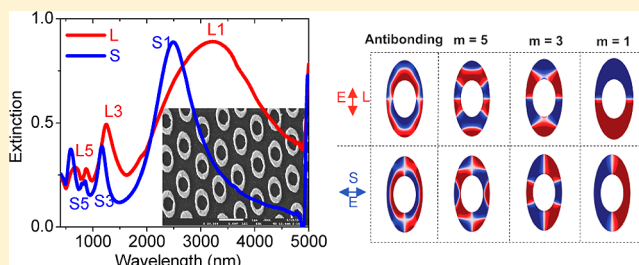
[†]Department of Chemistry, Texas A&M University, P.O. Box 30012, College Station, Texas 77843, United States

[‡]Department of Physics and Astronomy, Rice University, 6100 Main Street, Houston, Texas 77005, United States

S Supporting Information

ABSTRACT: Herein, a new and facile patterning method is demonstrated for the scalable fabrication of gold elliptical rings (ERs) in a controlled manner over large areas. In this method, well-ordered hexagonally arrayed polystyrene (PS) rings, fabricated by colloidal lithography, were used as masters to generate poly(dimethylsiloxane) (PDMS) stamps with circular apertures. The stamps were then stretched and utilized as molds for creating elliptical PS rings by a capillary filling process. Through subsequent reactive ion etching and chemical wet-etching, the elliptical PS rings could be readily transferred into an underlying gold film, leading to the formation of gold ERs. Since the aspect ratio (AR) of the elliptical PS rings could be controlled by varying the applied strain during the capillary filling process, gold ERs with different ARs could be fabricated in a scalable manner. The optical properties of the gold ERs were characterized by UV-vis/NIR and IR extinction measurements. The ERs exhibited only odd modes of polarization-dependent plasmonic resonances at normal incidence. The experiments and corresponding theoretical studies illustrated that all resonant modes could be tuned across a broad spectral range from the visible to the mid infrared (550–4700 nm) by simply varying the AR of the ERs. Moreover, the experimental data were confirmed by COMSOL simulations.

KEYWORDS: Elliptical nanorings, colloidal lithography, nanofabrication, surface plasmon, symmetry breaking, multipolar resonance



The interaction of metallic structures with electromagnetic radiation depends strongly on a particle's geometry, which is associated with localized surface plasmon resonances (LSPR). Specifically, the effects of size, periodicity, and morphology have stimulated substantial interest in experimental and theoretical research, which in turn has led to a wide range of applications, including chemical and biological sensors,^{1–3} photonics,⁴ surface-enhanced spectroscopy,^{5–9} and the development of metamaterials.^{10–12} One of the challenges is to widely tune the LSPR for specific applications. For example, it has been found that peak intensities from surface enhanced Raman spectroscopy (SERS) and surface enhanced infrared absorption spectroscopy (SEIRAS) are dependent on the particular geometries of the nanostructures. Generally, optimal enhancement and signal generation can be achieved when the LSPR resonances of the nanostructures are tuned to match the excitation wavelength of adjacent molecules of interest.^{8,13} In addition, for planar nanostructures, only dipolar resonances could be excited at normal incidence. However, higher order resonances have more uniform E-field distributions due to a larger number of nodes, which can be particularly useful for SERS measurements and sensing applications.¹⁴ Therefore, it is highly desirable to generate nanostructures with multiple, highly tunable, and predictable LSPR resonances over a wide wavelength range.

In previous studies, considerable effort was put into understanding the behavior of circular nanorings. This is because of the ease of fabrication and tunable plasmonic properties, which are desirable for a variety of applications.^{15–24} For example, nanorings have a uniformly enhanced electric field inside a circular cavity, which has been shown to be suitable for biosensor development.^{15,17} On the other hand, rings with reduced symmetry (symmetry-breaking) have been fabricated by the introduction of gaps or asymmetric widths into the symmetric ring structure. Such reduced symmetry should exhibit unique optical and magnetic properties that are not available with symmetric structures. A common asymmetry geometry is the split-ring, first proposed by Pendry et al.,²⁵ which has prompted a wide range of applications.^{2,9,26,27} Recently, Nordlander et al. proposed ring structures with asymmetric gaps, which exhibit asymmetric Fano resonances and unusually large LSPR sensitivity.^{28,29} Such elements could be potentially applied in new types of optical devices and sensors. An alternative strategy for introducing asymmetry into circular rings involves elongating them into elliptical rings. ERs have shown unique properties in magnetic materials compared with their symmetric ring counterparts.³⁰

Received: June 29, 2012

Revised: August 5, 2012

Published: August 13, 2012

To the best of our knowledge, the LSPR properties of metallic ERs have not yet been investigated. This is because it has been a formidable task to fabricate elliptical nanostructures with high geometrical tunability in a well-controlled manner over macroscopic areas. Electron-beam lithography (EBL) and ion beam milling have been employed to generate ERs.^{30,31} However, EBL is an expensive and slow process, which hampers its widespread application and requires large-scale fabrication facilities. Recently, ERs have also been fabricated by capillary force lithography, in which PDMS stamps with elliptical features (holes or dots) were used as templates.³² However, this method required the preparation of stamps with elliptical features, which still relied on EBL. As such, finding a simpler and more versatile fabrication method for ER production would be highly desirable.

Colloidal lithography (also known as nanosphere/microsphere lithography) has emerged as a simple, cost-effective, and versatile technique for rapid, large-area patterning.^{33,34} Numerous different structures, such as disks,^{35,36} circular rings,^{33,37–40} triangles,⁴¹ and crescents,²⁶ have been generated using spherical colloids as templates.^{42–46} Until now, ERs have not been made by colloidal lithography. One possible method to fabricate ERs might be to use prepared elliptical colloids as templates in a fashion similar to the process involved to generate circular rings, which involves using spherical colloids as templates. However, this would require the synthesis of elliptical nanoparticles and currently it is still challenging to assemble elliptical building blocks into ordered patterns over large areas.^{47–49}

Herein, we developed a scalable method for ER production over large areas. The idea is based on templates of spherical colloids in highly ordered arrays. By templating such arrays into stretchable PDMS elastomers,^{50–52} this method allowed for the generation of ERs with varying aspect ratios by using a single PDMS stamp. The plasmonic resonances of these structures could be tuned in a predictable manner as the aspect ratio of the ERs was varied. Moreover, varying the ring widths along the perimeter of the ERs allowed multipolar resonances to be excited. These ranged in frequency from the visible to the mid-IR and were highly polarization dependent.

Fabrication of ERs. Figure 1 outlines the procedure for fabricating ERs. In this method, circular polymer nanorings were fabricated using colloidal lithography analogous to previous investigations.³⁷ However, in previous work, the nanorings were not fabricated in ordered arrays because hydrophobic polystyrene (PS) films (water contact angle: $\sim 90^\circ$) were used as substrates for silica nanoparticle deposition and assembly. In order to obtain a hexagonally arrayed pattern, we modified the previous procedure slightly. Specifically, before depositing silica spheres, the PS film (molecular weight: $M_w \sim 97400$; thickness: ~ 100 nm) was treated with an O_2 plasma for ~ 30 s, which rendered the surface hydrophilic (water contact angle: $\sim 0^\circ$). The short period of plasma treatment reduced the film thickness by ~ 40 nm but had no discernible effect on the subsequent capillary rise of PS along the silica spheres. The singular noticeable change was the formation of large-scale, well-ordered arrays.

To form an array of nanoparticles, a $20 \mu\text{L}$ aqueous droplet containing 2.0 wt % of $1 \mu\text{m}$ silica particles was spread onto the O_2 plasma-treated PS film and spontaneously formed an ordered array upon drying (Figure 1a). Since only the bottom layer of particles was responsible for the formation of patterns in the PS substrate, particle deposition was controlled to be

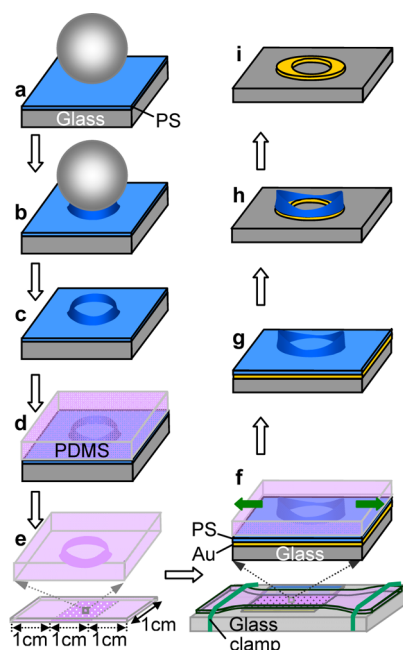


Figure 1. Schematic procedure for fabricating gold ERs. (a) Depositing silica particles ($1 \mu\text{m}$ in diameter) on an O_2 plasma treated PS film on glass ($\sim 1 \text{ cm} \times 1 \text{ cm}$). (b) Annealing the substrate above the T_g of PS. (c) Sonicating off silica particles. (d) Casting a PDMS film on the substrate surface followed by curing. (e) Releasing the PDMS film from the substrate and cutting the PDMS film into a rectangular sheet ($1 \text{ cm} \times 3 \text{ cm}$) with the patterned area in the middle (bottom panel). (f) Stretching the PDMS film and contacting it with a PS/Au/glass substrate and annealing at 130°C for 10 min. The 3 cm long PDMS sheet, containing the patterned PDMS stamp in the middle, is used for stretching in order to make sure the aspect ratios of the stretched nanostructures are uniform in the middle (bottom panel). (g) Releasing the PDMS sheet to form elliptical PS rings. (h) Treating the substrate by RIE to remove the residual PS film and subsequent wet-etching of the uncovered portions of the Au film. (i) Removing the remaining PS by O_2 plasma treatment.

somewhat thicker than one monolayer to ensure that the PS film was totally covered by silica spheres. The sample was then annealed above the glass transition temperature ($T_g \sim 100^\circ\text{C}$) of the PS film ($T = 130^\circ\text{C}$) for 10 min, leading to the formation of circular rings along the contours of the colloidal spheres (Figure 1b). After the silica particles were removed by sonication in a 1:1 volume mixture of water and ethanol, circular impressions were left behind in the PS film (Figure 1c). These structures were used to create a PDMS stamp with annular apertures (Figure 1d). The PDMS mold was then removed (Figure 1e) and stretched by applying a uniaxial strain. Next, the strained elastomer was placed into contact with an unpatterned PS film on a Au coated planar glass slide (~ 50 nm PS/ 50 nm Au/ 5 nm chromium/glass) (Figure 1f).

In order to facilitate conformal contact between the stretched PDMS sheet and the PS film, the thickness of the PDMS mold was kept to ~ 1 mm. Upon annealing the sample at 130°C for 20 min, PS filled into the cavities of the stretched mold by capillary forces (Figure 1f). At this point, the PDMS sheet was released from the substrate, leaving behind elliptical ring patterns (Figure 1g). To transfer this pattern to an underlying Au layer, the sample was treated by reactive ion etching (RIE) to remove the residual PS film and subsequent wet chemical etching to remove the exposed portions of the Au layer (Figure 1h). Finally, the remaining PS was removed by O_2 plasma

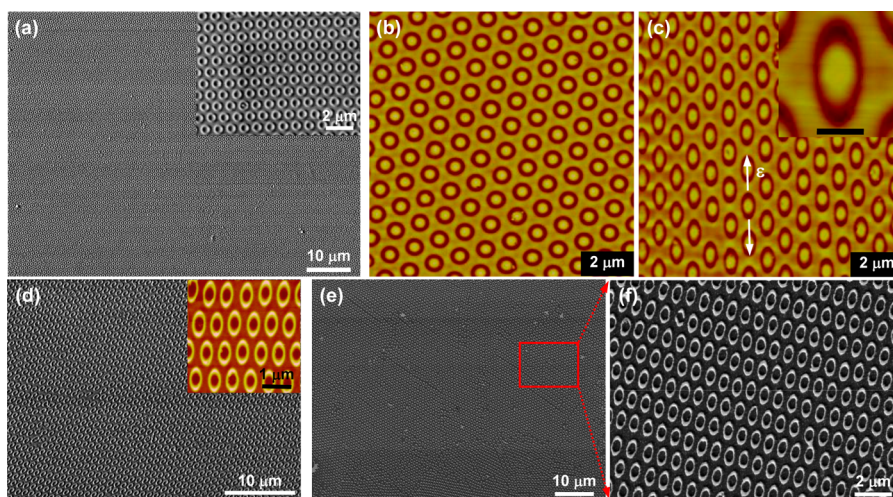


Figure 2. (a) SEM image of circular PS rings. The inset is a high-resolution image. (b and c) AFM images ($10\ \mu\text{m} \times 10\ \mu\text{m}$) of the PDMS sheet replicated from circular PS rings before and after stretching, respectively. The high-resolution inset image in part c (scale bar: 500 nm) shows that the width of the aperture along the long axis is larger than that along the short axis. The white arrows indicate the strain direction. (d) PS ERs generated by using the stretched PDMS sheet as a mold. The inset is an AFM image ($5\ \mu\text{m} \times 5\ \mu\text{m}$) of the PS ERs. (e) SEM image of Au ERs on a glass substrate. (f) High resolution SEM images of part e.

treatment (~ 3 min), leading to the formation of Au ERs on the glass substrate (Figure 1i).

Figure 2a shows an SEM image of circular PS rings obtained after annealing silica particles on a PS film at $130\ ^\circ\text{C}$ for 10 min. The silica particles were removed before imaging. The hexagonal PS ring array was well ordered over macroscopic areas ($\sim 1\ \text{cm} \times 1\ \text{cm}$). The PDMS stamp replicated from the circular PS rings exhibited depressed circular apertures, as seen by AFM (Figure 2b). When the PDMS stamp was stretched under a 40% strain (i.e., an elongation of 40%), the circular apertures were transformed into ellipses (Figure 2c). The SEM image in Figure 2d demonstrated that elliptical PS rings could be generated successfully by using the stretched PDMS stamp as a template. The inset in this figure is an AFM image of the same substrate. After O_2 RIE and subsequent wet etching, highly ordered arrays of Au elliptical rings were formed on the glass substrate, as shown over a large area (Figure 2e) and close-up SEM image (Figure 2f).

Controlling the Aspect Ratio. The method described in Figures 1 and 2 can be tuned over a wide range of geometries by varying the parameters of the experiment. First, by using silica particles with a fixed size, varying the annealing time, temperature, conditions of RIE, and chemical wet etching could be exploited to control the diameter and width of the circular rings^{32,53} and hence the corresponding widths of the ERs. Of course, the size, inter-ring distance, and periodicity of the ER elements can also be tuned by changing the size of the silica particles. It should be noted that, once a PDMS stamp with circular apertures is fabricated (Figure 1d), it can be employed to create ERs of varying aspect ratios by tuning the applied strain. Moreover, a single PDMS mold can be used repeatedly. To demonstrate this, we used the mold from Figure 2b to generate all of the ERs described below.

Figure 3a shows that Au ERs with different aspect ratios (ARs) could be generated by simply applying varying strains (ϵ) to a single PDMS stamp. The AR of Au ERs is defined by the ratio of the outer diameter along the long axis (D_L) to that along the short axis (D_S) (schematic diagram in Figure 3a). Without applied strain, circular rings (AR = 1.0) were produced. As ϵ increased from 10, 30, 40, to 50%, the AR

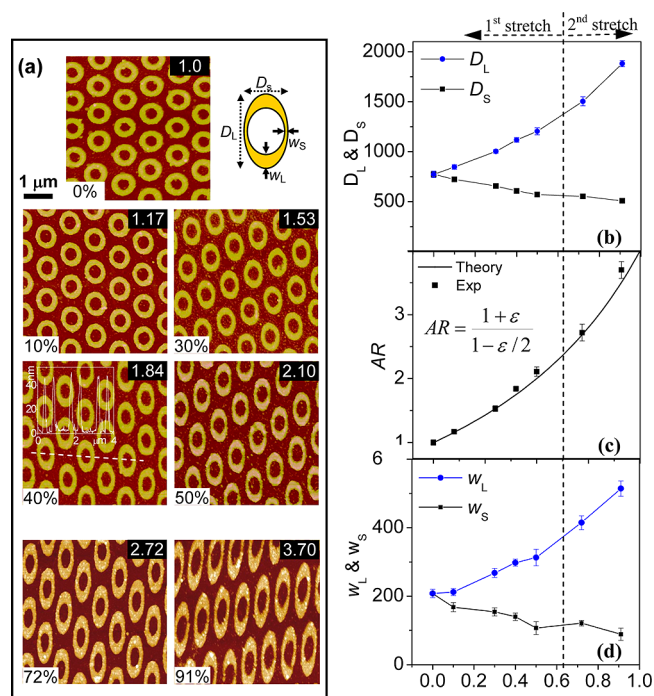


Figure 3. Control of the aspect ratios (ARs) of gold ERs. (a) AFM images ($5\ \mu\text{m} \times 5\ \mu\text{m}$) of the gold ERs with different ARs (1.0, 1.17, 1.53, 1.84, 2.11, 2.72, and 3.70). The first five images were generated under strains of 0, 10, 30, 40, and 50%, and the bottom two were generated by using second-generation PDMS stamps replicated from the PS ERs with an AR of ~ 1.84 . Scale bar: $1\ \mu\text{m}$. The schematic diagram shows the parameters of the ERs. The line profile for an AR of 1.84 shows that the height of the Au structures is ~ 45 nm. (b–d) Plots of the outer diameters (D_L and D_S), AR values of Au ERs, and widths (w_L and w_S), respectively, as a function of ϵ . The solid line in part c is the theoretic fit to the inset equations. The dashed line across the plots (b–d) is used to show that the data points to the left (right) side are obtained from the first (second) stretch.

increased from 1.17, 1.53, 1.84, to 2.10, respectively. The maximum strain that could be applied on the PDMS sheet (i.e.,

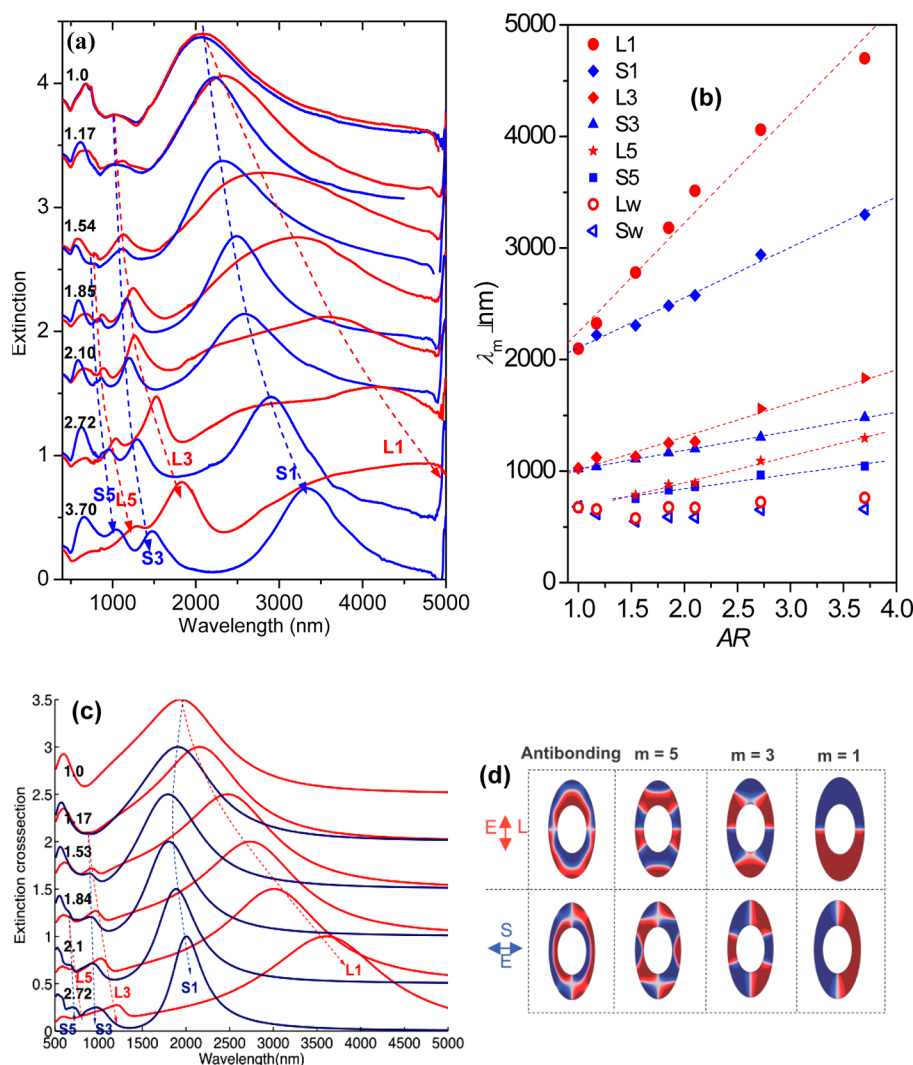


Figure 4. (a) Extinction spectra of the ERs with the ARs of ~ 1.0 , 1.17 , 1.53 , 1.84 , 2.10 , 2.72 , and 3.70 , respectively, for L (red) and S (blue) polarizations. (b) The wavelength, λ_m , of the resonance peaks of different modes ($m = 1, 3, 5$, and antibonding modes L_w and S_w) and polarizations (S and L) versus AR. (c) Comsol simulation of the extinction spectra of ERs with AR from 1.0 to 2.72 for L (red) and S (blue) polarizations. (d) Charge distribution profiles of the corresponding resonances for AR = 2.10 in part c. The dashed lines in parts a and c are used to highlight the varying position of the resonance peaks of the same order of mode and polarization with increasing AR.

the maximum elongation of PDMS at the breaking point) was $\sim 50\%$. This is smaller than the values that have been reported previously.^{54,55} The difference is that the present PDMS stamp is stretched and held in place at 130°C instead of room temperature. Generally, the elongation of PDMS at its breaking point decreases with increasing temperature.⁵⁵

One strategy to further increase the AR could involve lowering the annealing temperature by using a lower molecular weight polymer (i.e., decreasing T_g). Herein, a second-generation PDMS stamp was employed instead.⁵² To do this, ERs in PS with AR ~ 1.8 were used as masters and applied to a new PDMS mold. Thus, the new unstretched PDMS template contained elliptical apertures with AR ~ 1.8 , and after stretching along the direction of the long axis, elliptical apertures with greater ARs were generated. The bottom two AFM images in Figure 3a show Au ERs with ARs of 2.72 and 3.70 that were formed by applying a strain of ~ 30 and $\sim 50\%$, respectively, to the second-generation stamp. An iterative process could be employed if even higher aspect ratios were desired.

The increase of AR is the result of increasing D_L while decreasing D_S as a function of strain, ϵ (Figure 3b). Here, ϵ is defined as $\epsilon = [(D - D_0)/D_0] \times 100\%$, where D_0 and D are the diameters of the apertures in the PDMS sheet before and after applying the stain, respectively. Note that D can be used for either D_L or D_S . When a stain, ϵ , is applied to a templated PDMS sheet, the initial diameter, D_0 , of the circular aperture along the direction of the applied strain increases to $D_L = (1 + \epsilon)D_0$. On the other hand, D_S is reduced to $D_S = (1 - \nu\epsilon)D_0$. This later shrinkage is caused by a Poisson contraction⁵⁶ of PDMS, and ν is the Poisson ratio of PDMS (~ 0.5). As a result, the AR of the elliptical apertures (Figure 3c) can be written as

$$\text{AR} = \frac{1 + \epsilon}{1 - \epsilon/2} \quad (1)$$

which can also be approximated as the AR of the resulting Au ERs. For the second-generation PDMS stamp, the resulting AR should be

$$AR = \frac{1 + \varepsilon_1}{1 - \varepsilon_1/2} \cdot \frac{1 + \varepsilon_2}{1 - \varepsilon_2/2} \quad (2)$$

where ε_1 and ε_2 are the strains applied in the first and second rounds of the stretching processes, respectively. Inserting the values of ε_1 and ε_2 into eq 2 results in theoretical ARs of 2.68 and 3.50 after second generation stretching (bottom two images in Figure 3a). This agrees reasonably well with the measured values (~ 2.72 and ~ 3.70). For simplicity, the Au ERs generated by using second-generation PDMS stamps can be considered to be generated by a one-time stretching under an effective strain (ε_{eff}):

$$\frac{1 + \varepsilon_1}{1 - \varepsilon_1/2} \cdot \frac{1 + \varepsilon_2}{1 - \varepsilon_2/2} = \frac{1 + \varepsilon_{\text{eff}}}{1 - \varepsilon_{\text{eff}}/2} \quad (3)$$

For the ARs of 2.72 and 3.70, ε_{eff} is ~ 72 and $\sim 91\%$, respectively. Plotting a theoretical curve from the calculated AR due to the strain shows that all the experimental values agree well with this model (Figure 3c).

It can be readily observed that the ring width of the ERs is not uniform along the perimeter of the ERs. Indeed, the width reaches a minimum, w_s , normal to the stretching direction and a maximum, w_L , parallel to it (schematic diagram, Figure 3a). This width difference, which results at the PS templating step, is caused by strain-induced elongation/contraction of the long/short axes. While the apertures at the long axis are stretched, those at the short axis are compressed due to Poisson contraction. This leads to much of the width difference. Moreover, the inner PDMS circles are unattached from the larger matrix being stretched. As such, they deform less than the surrounding region, which further increases the difference between w_L and w_s (see the Supporting Information). The resulting width of the Au ERs can be tuned by several processes, including capillary filling by the PS film, O_2 RIE, and wet etching. Since all the lithographic conditions were kept constant as the strain was increased, w_L and w_s also increased and decreased, respectively, with ε in the present case (Figure 3d).

Optical Properties of the ERs. The LSPR behavior of ERs with varying ARs were characterized by UV-vis/NIR (400–3000 nm) and FTIR (2000–5000 nm) at normal incidence using polarized light. Spectra from these two separate spectrometers were combined together to create continuous spectra from 400 to 5000 nm. The overlap region (from 2000 to 3000 nm) was used for normalization. We found that the extinction spectra of the ERs were highly repeatable (see Figure S2 in the Supporting Information), implying that ERs fabricated by this method were uniform over the whole substrate and reproducible from sample to sample.

Figure 4a shows the extinction spectra (400–5000 nm) of Au ERs with AR values of 1.0, 1.17, 1.53, 1.84, 2.10, 2.72, and 3.70. The spectra in red are from light with the electric field polarized along the long axis, while the blue spectra are for light polarized along the short axis. As expected, the spectra of circular rings (AR = 1.0) are identical for the two polarizations (Figure 4a). The circular rings exhibited three distinct peaks at 2100, 1022, and 650 nm. The plasmon modes of metallic ring structures can be classified according to their azimuthal symmetry m (where m ranges from 1 to infinity) and the relative charge alignment on the inner and outer surfaces (symmetric or antisymmetric) of the ring wall. According to previous studies,^{15,23,24} circular rings generally exhibited two resonance peaks: a symmetric bonding dipolar and an

asymmetric antibonding plasmon mode. The bonding dipolar mode with its electric field extending over the whole structure is highly tunable and depends sensitively on the geometrical parameters of the structure.⁵⁷ In contrast, the antibonding mode with its electric field localized within the ring wall is only weakly tunable and depends primarily on the ring width w . The strong peak at 2100 nm has been assigned to the symmetric dipolar resonance (or the mode-1 resonance: $m = 1$), while the peak at 650 nm was ascribed to the antibonding resonance along the width of the circular rings (λ_w).

In the present work, an unexpected weak peak was also found near 1022 nm and has not been previously assigned. This mode is barely visible for circular rings at normal incidence and is a dark higher order multipolar resonance.²² Such dark-mode resonances should become significantly more intense when the symmetry of the nanostructures is broken.^{16,28,58} For example, it has been recently reported that asymmetric theta-shaped ring-rod Au nanostructures⁵⁹ and nanorings with asymmetric widths²⁸ exhibited dark-mode resonances at normal incidence. In the present case, two possible symmetry-breaking factors may contribute to the appearance of the 1022 nm peak. First, the ring width of circular rings may not be perfectly uniform along the perimeter of the rings due to fabrication defects, which may result in the excitation of dark mode resonances.²² Second, the surfaces of Au nanorings will not be perfectly smooth after chemical wet etching, which may also result in symmetry breaking and therefore enable excitation of dark-mode resonances at normal incidence.⁵⁸

While circular rings gave rise to polarization independent extinction spectra, the spectra from the ERs exhibited significant polarization dependence (Figure 4a). For ERs, there are polarizations along both the long and short axes, which are referred to as “L” and “S” polarization, respectively. Like circular rings, the ~ 650 nm peaks in the spectra for all the ERs can be attributed to the antibonding resonances along the width of the structures.

The lowest energy features can be assigned to bonding dipolar resonances of the ERs and are labeled as S1 and L1 in Figure 4a. Both modes continuously red-shifted as the aspect ratio was increased. In addition to the dipolar bonding and antibonding resonances, ERs also exhibited higher order resonances for each polarization. For ERs with an AR of 1.17, only one higher order resonance appears for each polarization, and is labeled L3 and S3, respectively. Interestingly, as the AR was increased to 1.54 and beyond, one additional weak resonance was found for each polarization, and is labeled L5 and S5. Similar to the dipolar resonances, these high-order resonances also red-shifted when the polarization was switched from S to L ($\lambda_{S3} < \lambda_{L3}$ and $\lambda_{S5} < \lambda_{L5}$). Moreover, the observed intensities of the higher order resonances increased with increasing aspect ratio. As noted above, higher order resonances should be the result of symmetry breaking. This may be attributed to two factors: one is the anisotropic shape of the ERs, and the other is the difference between w_L and w_s , as shown in Figure 3d. As the AR increased, the extent of symmetry-breaking increased, leading to increasing intensities of the higher order resonances. In addition, the resonances for the same order of mode and polarization (L1, S1, L3, S3, L5, and S5) red-shifted with increasing AR, as revealed by the dashed arrows in Figure 4a.

The extinction maxima as a function of AR for the spectra in Figure 4a are plotted in Figure 4b. As can be seen, the resonance wavelengths increased almost linearly with increasing

AR. However, the antibonding resonances did not show a significant red-shift by increasing the AR. It should be noted that all the above resonances are assigned odd azimuthal mode numbers $m = 1, 3$, and 5 . Similar phenomena have been observed in nanowires, in which only odd-mode resonances were observed at normal incidence.^{58,60} This is in agreement with theory, as discussed below. Even mode resonances can also be excited but require off normal incidence excitation.²²

To analyze the experimental results in Figure 4a and b, we performed COMSOL simulations of the optical cross section of a single ER. Figure 4c shows the simulated spectra for an ER with ARs ranging from 1.0 to 2.72. The charge distribution profiles of the corresponding resonance peaks for AR = 2.10 are shown in Figure 4d. The antibonding resonances in the simulated spectra are in good agreement with the experimental data. Their charge distribution profiles (left two panels in Figure 4d) confirm the antisymmetric alignment expected for antibonding modes. For circular rings, only the dipolar resonance was observed. By contrast, dipolar resonances and higher order resonances were observed in the spectra of ERs for both polarizations. On the basis of the charge distribution profiles of the dipolar and high-order resonances, the order of the resonance modes (m) can be calculated to be half of the number of nodes (i.e., $m = n/2$) in the ERs. For example, because the higher order resonance in the L-polarization has six nodes along the perimeter of the ER, the resulting order of mode is 3, which is consistent with the assigned mode in Figure 4a.

The simulation data in Figure 4c show that all dipolar and multipolar resonances, except S1 resonances, red-shift with the increase of AR. This is mostly consistent with the experimental results. However, the S1 resonances in the simulation first blue-shifted slightly and then red-shifted as the AR increased further. This will be qualitatively explained below using a simple standing-wave model. Moreover, the resonances in the simulations, especially the S1 and high-order resonances, exhibited clear blue-shifts compared to the experimental results. There are several reasons for this deviation from the experimental data. First, the experimental data were measured from 2D arrays of ERs, while the simulations only calculated extinction spectra from a single ER. The coupling between ER elements in the experiments could induce the red-shift of the plasmonic resonances, which has been observed for circular nanorings.¹⁹ Moreover, this coupling effect strongly depends on the pitch of the 2-D arrays or the gap between adjacent rings. For the ER arrays, the gap distance increased by $(1 + \varepsilon)$ along the long axis but decreased by $(1 - \varepsilon/2)$ along the short axis. This may explain why the S1 resonances in the simulation blue-shifted as compared to the resonances in experiments, while the L1 resonances almost matched the experimental data. Second, the roughness of the Au surface in the experiments could produce a red-shift of resonances, which was not taken into account in the simulations. Indeed, this phenomenon has been observed in Au nanodots⁶¹ and nanocrescents.⁶² Third, the glass substrate in the experiment was not included in the simulation. Finally, the cross sections of the ERs were not perfectly rectangular as assumed in the simulations. Generally, due to isotropic wet etching of Au, they were narrow on the top and wide at the bottom, resulting in trapezoidal or even triangular shapes (see Figure S2b,c in the Supporting Information). The asymmetric cross-sectional shapes could also cause red-shifting of the resonances.²³

In order to quantitatively understand the shift of the resonance peaks, we employed a simple standing-wave model originally introduced to analyze the plasmonic resonances of a linear antenna of finite length l .^{63,64}

$$L = m\lambda_m/2n \quad (4)$$

In this expression, λ_m is the wavelength of the resonance of mode index m and n is the refractive index of the surrounding medium. This simple model has also been extended to other metallic ring structures which are then considered as linear antennas of lengths equal to the circumference of the ring.^{11,16,65} In the most general case, the multiple plasmon resonances of a closed ring-like structure such as an ER can be obtained from a modified standing wave model:¹¹

$$l_{\text{eff}} = \frac{m(\lambda_m + \lambda_0)}{2n_{\text{eff}}} \quad (5)$$

where l_{eff} is the effective length of the structure in the polarization direction and λ_0 depends only on the geometric structure.¹¹

LSPR resonances of closed square rings of total perimeter lengths C have been shown to be independent of polarization because the effective length, $l_{\text{eff}} = C/2$, is independent of polarization.⁶⁵ The polarization-independent spectra of the closed circular rings (AR = 1.0) in Figure 4a confirm this finding. By contrast, the spectra from ERs were polarization dependent. This is due to the fact that l_{eff} in eq 5 is different in the L and S directions. For an elliptical ring with long and short axes diameters of D_L and D_S , the half length of the perimeter is

$$l = (\pi/4)\sqrt{2(D_L^2 + D_S^2) - (D_L - D_S)^2}/2 \quad (6)$$

For the L polarization, the electrical field (E) is parallel to the long axis of the ERs and the electrical currents oscillate between the two ends of the long axis (schematic diagram in Figure 5a). Therefore, the effective length l_L in the L direction can be calculated by substituting D_S by the inner diameter at the short axis ($D_S - 2w_S$):

$$l_L = (\pi/4)\sqrt{2(D_L^2 + (D_S - 2w_S)^2) - (D_L - (D_S - 2w_S))^2}/2 \quad (7)$$

Similarly, the effective length l_S in the S direction can be calculated by substituting D_L by the inner diameter along the long axis ($D_L - 2w_L$):

$$l_S = (\pi/4)\sqrt{2((D_L - 2w_L)^2 + D_S^2) - ((D_L - 2w_L) - D_S)^2}/2 \quad (8)$$

The values of l_L and l_S are plotted as a function of AR in Figure 5a. As expected, l_L is larger than l_S because $w_L > w_S$. Therefore, as expected from eq 5, the resonances red-shifted when the polarization was switched from S to L.

In order to further confirm that this red-shift was caused by the nonuniform ring width, we simulated the extinction spectra of ERs (AR = 1.84) of a uniform ring width of 50 nm. As expected, the spectra were almost polarization independent (Figure S3, Supporting Information). Figure 5a also shows that l_L increases monotonously with increasing AR, which explains why λ_L red-shifts with increasing AR, as shown in Figure 4c. In contrast, l_S first decreases with increasing AR with a minimum for AR = 1.54, and then undergoes a monotonous increase for larger AR. This is consistent with the trend for the simulated λ_{S1} (Figure 4c), where the S1 resonance blue-shifted when the AR was increased from 1.0 to 1.54 and then red-shifted as the

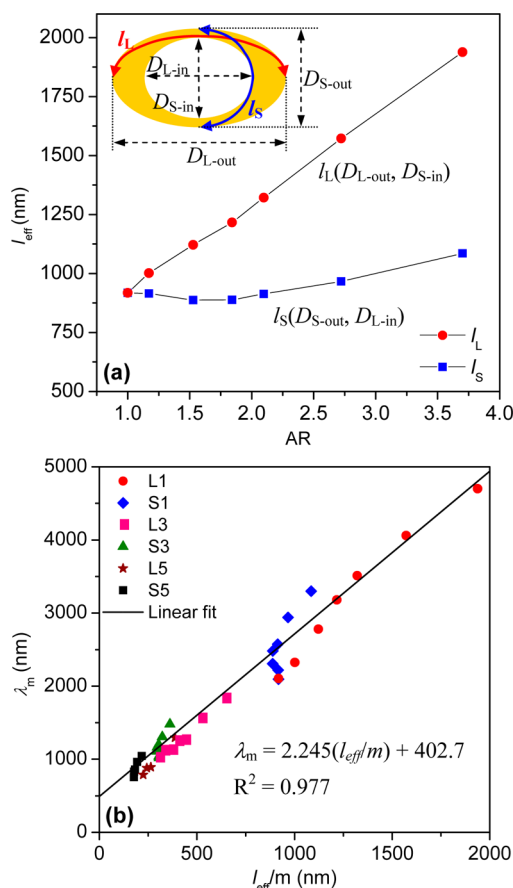


Figure 5. (a) Plot of the effective path length l_{eff} (l_L and l_S) of the currents in ERs induced in two polarizations (L and S) as a function of AR. The schematic diagram shows that l_L can be calculated on the basis of D_{L-out} and D_{S-in} and l_S can be calculated on the basis of D_{S-out} and D_{L-in} . (b) Plot of wavelengths of multiple resonant peaks of different modes ($m = 1, 3$, and 5) and polarizations (L and S) as a function of l_{eff}/m . The solid line is a linear fit.

AR value was further increased. Again, both the standing wave model and the simulations were based on a single ER. As a result, this clearly explains the variation of dipolar resonances in the simulation. However, as noted above, the coupling between periodic ERs can also cause a red-shift of the resonance. To demonstrate this, we ran an additional simulation to compare the resonances of a single ER with a periodic ER array (Figure S4, Supporting Information). As expected, the resonances for the ER array were red-shifted with respect to those for a single ER.

In order to further understand the resonances, we plotted the experimental resonance peaks (λ) as a function of l_{eff}/m (Figure 5b). As expected from eq 5, λ followed a linear relationship with l_{eff}/m . This agreement suggests that the generalized standing wave model can be used as a simple and quantitative description of the polarization dependent resonant peaks of the ERs. Moreover, the resonances of the ERs could be simply predicted from the dimensions of the ERs, which is key for sensor design. Additionally, n_{eff} was derived from the slope of Figure 5b and eq 3 to be 1.123. As the gold ERs were surrounded by two media, the glass substrate and air with refractive indices of 1.47 and 1.00, respectively, this value is within a reasonable range.

Conclusions. In summary, we have demonstrated a simple patterning technique based on colloidal lithography to fabricate

well-ordered PS and Au ERs over large areas ($\sim 1 \text{ cm}^2$ in this paper) in a highly controlled manner. One unique advantage of this method was that it enabled the scalable fabrication of Au ERs with varying AR by simply tuning the strain. This previously required using different molds in soft lithography or employing EBL. Due to the ability to control the aspect ratio of the rings and therefore the plasmonic resonance positions, our method provides an effective platform for LSPR sensor design in a wavelength range from the optical to the infrared. Additional applications of these structures may involve optical coatings and filters. In fact, some extinction resonances are quite narrow and can be tuned to block incident light at specific wavelengths. However, some resonance peaks are relatively broad, which may be attributed to the imperfect lattice ordering of the self-assembled hexagonal arrays and the existence of the Cr adhesive layer.^{66,67} By fine-tuning the self-assembly process⁶⁸ and using an alternative (e.g., (3-mercaptopropyl)-trimethoxysilane) adhesive layer,⁶⁷ these resonances might be considerably narrowed. Finally, since this technique is not limited to Au structures, magnetic ERs could also be generated by simply introducing magnetic materials into the polymer film³⁷ or the substrate,³² which may also be of practical value in magnetic device applications.

■ ASSOCIATED CONTENT

Supporting Information

Experimental and simulation details, discussions about the effect of unattached inner PDMS circles on ring width, AFM images of ERs and corresponding spectra from two spots and two samples, simulation for coupling effect, simulated spectra of ERs with thin and uniform widths. This material is available free of charge via the Internet at <http://pubs.acs.org>.

■ AUTHOR INFORMATION

Corresponding Author

*E-mail: cremer@mail.chem.tamu.edu.

Notes

The authors declare no competing financial interest.

■ ACKNOWLEDGMENTS

P.S.C. and Y.C. thank the Norman Hackerman Advanced Research Project (NHARP, 010366-0040-2009) from the Texas Higher Education Coordinating Board and the Office of Naval Research (N00014-08-0467) for funding. P.N. and Y.L. were supported by the Robert A. Welch foundation under grant C-1222 and the Office of Naval Research under grant N00014-10-0989.

■ REFERENCES

- (1) Stewart, M. E.; Anderton, C. R.; Thompson, L. B.; Maria, J.; Gray, S. K.; Rogers, J. A.; Nuzzo, R. G. *Chem. Rev.* **2008**, *108*, 494–521.
- (2) Clark, A. W.; Glidle, A.; Cumming, D. R. S.; Cooper, J. M. *J. Am. Chem. Soc.* **2009**, *131*, 17615–17619.
- (3) Liao, W.-S.; Chen, X.; Yang, T.; Castellana, E. T.; Chen, J.; Cremer, P. S. *Biointerphases* **2009**, *4*, 80–85.
- (4) Yan, R.; Gargas, D.; Yang, P. *Nat. Photonics* **2009**, *3*, 569–576.
- (5) Ko, H.; Singamaneni, S.; Tsukruk, V. V. *Small* **2008**, *4*, 1576–1599.
- (6) Stiles, P. L.; Dieringer, J. A.; Shah, N. C.; Van Duyne, R. P. *Annu. Rev. Anal. Chem.* **2008**, *1*, 601–626.
- (7) Banholzer, M. J.; Millstone, J. E.; Qin, L.; Mirkin, C. A. *Chem. Soc. Rev.* **2008**, *37*, 885–897.

- (8) Adato, R.; Yanik, A. A.; Amsden, J. J.; Kaplan, D. L.; Omenetto, F. G.; Hong, M. K.; Erramilli, S.; Altug, H. *Proc. Natl. Acad. Sci. U.S.A.* **2009**, *106* (19227–19232), S19227.
- (9) Bukasov, R.; Shumaker-Parry, J. S. *Anal. Chem.* **2009**, *81*, 4531–4535.
- (10) Shelby, R. A.; Smith, D. R.; Schultz, S. *Science* **2001**, *292*, 77–79.
- (11) Chen, C.-Y.; Wu, S.-C.; Yen, T.-J. *Appl. Phys. Lett.* **2008**, *93*, 034110.
- (12) Soukoulis, C. M.; Kafesaki, M.; Economou, E. N. *Adv. Mater.* **2006**, *18*, 1941–1952.
- (13) Yu, Q.; Guan, P.; Qin, D.; Golden, G.; Wallace, P. M. *Nano Lett.* **2008**, *8*, 1923–1928.
- (14) Sheridan, A. K.; Clark, A. W.; Glidle, A.; Cooper, J. M.; Cumming, D. R. S. *Appl. Phys. Lett.* **2007**, *90*, 143105.
- (15) Aizpurua, J.; Hanarp, P.; Sutherland, D. S.; Kall, M.; Bryant, G. W.; Garcia de Abajo, F. J. *Phys. Rev. Lett.* **2003**, *90*, 057401.
- (16) Nordlander, P. *ACS Nano* **2009**, *3*, 488–492.
- (17) Larsson, E. M.; Alegret, J.; Kaell, M.; Sutherland, D. S. *Nano Lett.* **2007**, *7*, 1256–1263.
- (18) Li, K.; Clime, L.; Tay, L.; Cui, B.; Geissler, M.; Veres, T. *Anal. Chem.* **2008**, *80*, 4945–4950.
- (19) Jiang, H.; Sabarinathan, J. J. *Phys. Chem. C* **2010**, *114*, 15243–15250.
- (20) Ye, J.; Shioi, M.; Lodewijks, K.; Lagae, L.; Kawamura, T.; Van Dorpe, P. *Appl. Phys. Lett.* **2010**, *97*, 163106.
- (21) Banaee, M. G.; Crozier, K. B. *Opt. Lett.* **2010**, *35*, 760–762.
- (22) Hao, F.; Larsson, E. M.; Ali, T. A.; Sutherland, D. S.; Nordlander, P. *Chem. Phys. Lett.* **2008**, *458*, 262–266.
- (23) Ye, J.; van Dorpe, P.; Lagae, L.; Maes, G.; Borghs, G. *Nanotechnology* **2009**, *20*, 465203.
- (24) Tsai, C.-Y.; Lu, S.-P.; Lin, J.-W.; Lee, P.-T. *Appl. Phys. Lett.* **2011**, *98*, 153108.
- (25) Pendry, J. B.; Holden, A. J.; Robbins, D. J.; Stewart, W. J. *IEEE Trans. Microwave Theory Tech.* **1999**, *47*, 2075–2084.
- (26) Shumaker-Parry, J. S.; Rochholz, H.; Kreiter, M. *Adv. Mater.* **2005**, *17*, 2131–2134.
- (27) Clark, A. W.; Cooper, J. M. *Adv. Mater.* **2010**, *22*, 4025–4029.
- (28) Hao, F.; Sonnefraud, Y.; Van Dorpe, P.; Maier, S. A.; Halas, N. J.; Nordlander, P. *Nano Lett.* **2008**, *8*, 3983–3988.
- (29) Luk'yanchuk, B.; Zheludev, N. I.; Maier, S. A.; Halas, N. J.; Nordlander, P.; Giessen, H.; Chong, C. T. *Nat. Mater.* **2010**, *9*, 707–715.
- (30) Chang, L. J.; Yu, C.; Chiang, T. W.; Cheng, K. W.; Chiu, W. T.; Lee, S. F.; Liou, Y.; Yao, Y. D. *J. Appl. Phys.* **2008**, *103*, 07C514.
- (31) Jung, W.; Castano, F. J.; Ross, C. A. *Phys. Rev. Lett.* **2006**, *97*, 247209.
- (32) Lee, S. Y.; Jeong, J.-R.; Kim, S.-H.; Kim, S.; Yang, S.-M. *Langmuir* **2009**, *25*, 12535–12540.
- (33) Zhang, J.; Li, Y.; Zhang, X.; Yang, B. *Adv. Mater.* **2010**, *22*, 4249–4269.
- (34) Zhang, J.; Yang, B. *Adv. Funct. Mater.* **2010**, *20*, 3411–3424.
- (35) Fredriksson, H.; Alaverdyan, Y.; Dmitriev, A.; Langhammer, C.; Sutherland, D. S.; Zaech, M.; Kasemo, B. *Adv. Mater.* **2007**, *19*, 4297–4302.
- (36) Hanarp, P.; Kaell, M.; Sutherland, D. S. *J. Phys. Chem. B* **2003**, *107*, 5768–5772.
- (37) Sun, Z.; Li, Y.; Zhang, J.; Li, Y.; Zhao, Z.; Zhang, K.; Zhang, G.; Guo, J.; Yang, B. *Adv. Funct. Mater.* **2008**, *18*, 4036–4042.
- (38) Liao, W.-S.; Chen, X.; Chen, J.; Cremer, P. S. *Nano Lett.* **2007**, *7*, 2452–2458.
- (39) McLellan Joseph, M.; Geissler, M.; Xia, Y. *J. Am. Chem. Soc.* **2004**, *126*, 10830–10831.
- (40) Chen, J.; Liao, W.-S.; Chen, X.; Yang, T.; Wark, S. E.; Son, D. H.; Batteas, J. D.; Cremer, P. S. *ACS Nano* **2009**, *3*, 173–180.
- (41) Haynes, C. L.; Van Duyne, R. P. *J. Phys. Chem. B* **2001**, *105*, 5599–5611.
- (42) Lu, Y.; Yin, Y.; Xia, Y. *Adv. Mater.* **2001**, *13*, 271–274.
- (43) Ho, C. C.; Keller, A.; Odell, J. A.; Ottewill, R. H. *Colloid Polym. Sci.* **1993**, *271*, 469–479.
- (44) Champion Julie, A.; Katere Yogesh, K.; Mitragotri, S. *Proc. Natl. Acad. Sci. U.S.A.* **2007**, *104*, 11901–11904.
- (45) Merkel, T. J.; Herlihy, K. P.; Nunes, J.; Orgel, R. M.; Rolland, J. P.; DeSimone, J. M. *Langmuir* **2010**, *26*, 13086–13096.
- (46) Hu, Y.; Ge, J.; Zhang, T.; Yin, Y. *Adv. Mater.* **2008**, *20*, 4599–4602.
- (47) Madivala, B.; Fransaer, J.; Vermant, J. *Langmuir* **2009**, *25*, 2718–2728.
- (48) Zhang, Z.-K.; Pfeleiderer, P.; Schofield, A. B.; Clasen, C.; Vermant, J. *J. Am. Chem. Soc.* **2011**, *133*, 392–395.
- (49) Grzelczak, M.; Vermant, J.; Furst, E. M.; Liz-Marzan, L. M. *ACS Nano* **2010**, *4*, 3591–3605.
- (50) Wang, T.; Li, X.; Zhang, J.; Ren, Z.; Zhang, X.; Zhang, X.; Zhu, D.; Wang, Z.; Han, F.; Wang, X.; Yang, B. *J. Mater. Chem.* **2010**, *20*, 152–158.
- (51) Wang, T.; Li, X.; Zhang, J.; Wang, X.; Zhang, X.; Zhang, X.; Zhu, D.; Hao, Y.; Ren, Z.; Yang, B. *Langmuir* **2010**, *26*, 13715–13721.
- (52) Wang, Y.; Merkel Timothy, J.; Chen, K.; Fromen Catherine, A.; Betts Douglas, E.; Desimone Joseph, M. *Langmuir* **2011**, *27*, 524–528.
- (53) Bruinink, C. M.; Peter, M.; Maury, P. A.; de Boer, M.; Kuipers, L.; Huskens, J.; Reinhoudt, D. N. *Adv. Funct. Mater.* **2006**, *16*, 1555–1565.
- (54) Choi, K. M.; Rogers, J. A. *J. Am. Chem. Soc.* **2003**, *125*, 4060–4061.
- (55) Ye, X.; Liu, H.; Ding, Y.; Li, H.; Lu, B. *Microelectron. Eng.* **2009**, *86*, 310–313.
- (56) Choi, W. M.; Song, J.; Khang, D.-Y.; Jiang, H.; Huang, Y. Y.; Rogers, J. A. *Nano Lett.* **2007**, *7*, 1655–1663.
- (57) Dutta, C. M. A.; Tamer, A.; Brandl, Daniel W.; Park, Tae-Ho; Nordlander, Peter J. *Chem. Phys.* **2008**, *129*, 084706/1–084706/9.
- (58) Neubrech, F.; Garcia-Etxarri, A.; Weber, D.; Bochterle, J.; Shen, H.; Lamy de la Chapelle, M.; Bryant, G. W.; Aizpurua, J.; Pucci, A. *Appl. Phys. Lett.* **2010**, *96*, 213111.
- (59) Habteyes, T. G.; Dhuey, S.; Cabrini, S.; Schuck, P. J.; Leone, S. R. *Nano Lett.* **2011**, *11*, 1819–1825.
- (60) Schider, G.; Krenn, J. R.; Hohenau, A.; Ditzlbacher, H.; Leitner, A.; Aussenegg, F. R.; Schaich, W. L.; Puscasu, I.; Monacelli, B.; Boreman, G. *Phys. Rev. B* **2003**, *68*, 155427.
- (61) Auguie, B.; Barnes, W. L. *Opt. Lett.* **2009**, *34*, 401–403.
- (62) Vogel, N.; Fischer, J.; Mohammadi, R.; Retsch, M.; Butt, H.-J.; Landfester, K.; Weiss, C. K.; Kreiter, M. *Nano Lett.* **2011**, *11*, 446–454.
- (63) Neubrech, F.; Kolb, T.; Lovrincic, R.; Fahsold, G.; Pucci, A.; Aizpurua, J.; Cornelius, T. W.; Toimil-Molares, M. E.; Neumann, R.; Karim, S. *Appl. Phys. Lett.* **2006**, *89*, 253104.
- (64) Novotny, L. *Phys. Rev. Lett.* **2007**, *98*, 266802.
- (65) Xu, Q.; Bao, J.; Rioux, R. M.; Perez-Castillejos, R.; Capasso, F.; Whitesides, G. M. *Nano Lett.* **2007**, *7*, 2800–2805.
- (66) Zheng, Y. B.; Juluri, B. K.; Mao, X.; Walker, T. R.; Huang, T. J. *J. Appl. Phys.* **2008**, *103*, 014308/1–014308/9.
- (67) Habteyes, T. G.; Dhuey, S.; Wood, E.; Gargas, D.; Cabrini, S.; Schuck, P. J.; Alivisatos, A. P.; Leone, S. R. *ACS Nano* **2012**, *6*, 5702–5709.
- (68) Zhang, J.; Li, Y.; Zhang, X.; Yang, B. *Adv. Mater.* **2010**, *22*, 4249–4269.